JOURNAL OF SPACECRAFT AND ROCKETS
Vol. 61, No. 1, January–February 2024

Engineering Notes

Observed High-Altitude Surface Erosion During the Mars Science Laboratory and Mars 2020 Landings

Jason Rabinovitch* and Soleil A. Santana†
Stevens Institute of Technology, Hoboken, New Jersey 07030
Christopher D. Karlgaard‡
Analytical Mechanics Associates, Inc., Hampton, Virginia 23666
Elizabeth T. Jens,§ Kathryn M. Stack,¶ and Daniel M. Turner**
Jet Propulsion Laboratory, California Institute of Technology, Pasadena, California 91009
Wesley A. Chambers†† and Manish Mehta‡‡
NASA Marshall Space Flight Center, Huntsville, Alabama 35812
and
Ashley M. Korzun§§
NASA Langley Research Center, Hampton, Virginia 23681

https://doi.org/10.2514/1.A35748

I. Introduction

THE altitudes at which surface erosion (or modification) was first observed for both the Mars Science Laboratory (MSL) mission, which successfully landed the Curiosity Rover, and the Mars 2020 mission, which successfully landed the Perseverance Rover, are summarized in Table 1. A similar altitude for surface modification is observed for both missions: ∼70 m above the surface during the MSL descent and ∼64 m during the Mars 2020 descent. This altitude is defined to be the distance from the surface to the Descent Stage center of mass, and at this point during the descent, the rover is still directly attached to the Descent Stage. Both of these spacecraft used a similar landing architecture and propulsion system during terminal descent, and both missions were also similar in size and mass, although the missions targeted different landing sites [1,2]. Generally speaking, both the MSL and Mars 2020 landing sites are composed of bedrock overlain by a thin layer (centimeters) of dust and regolith, and additional details can be found in [3–9].

This altitude gives information about when high-speed exhaust from the Mars lander engines (MLEs) [10] starts to modify the surface below the vehicle. These interactions, commonly referred to as plume-surface Interactions (PSI), have been studied and documented in detail for space exploration since the Apollo program (e.g., [11–15]), and have been a design driver for the landing systems used by many previous Mars missions [16–20]. In addition to the negative consequences of near-surface PSI (terminal descent), it is important to be able to predict the first point in a vehicle's trajectory where it is expected that the exhaust from a spacecraft's engines will begin to modify the surface.

To enable precision landing, systems that rely on visual or other optical feature tracking or radar may need to be operational at or below altitudes where surface alteration was first detected. Reliance on such capabilities without recognition of the potential for spoofing of radar [21] or degraded or even spurious sensor performance (e.g., obscure images used for Terrain Relative Navigation [22]) increases mission risk. Future Mars missions require landers that are significantly larger than MSL and Mars 2020. These vehicles will rely on larger, more powerful propulsion systems for terminal descent and landing while including stricter requirements for precision landing and hazard avoidance. Characterizing the altitude at which surface alteration is detectable permits a best-case-scenario baseline for these future missions. Furthermore, the altitude at which surface erosion begins can be used as a quantity of interest (QOI) to compare to modeling results. While high-fidelity modeling of PSI for spacecraft during landing remains a challenging endeavor (e.g., [23]), the surface erosion patterns observed during the MSL descent have already been compared to modeling results in [24] to see if surface erosion features that are observed in numerical simulations are similar to those observed during flight. However, the majority of previous published works focus on near-surface PSI, and do not consider the onset of erosion that occurs at a relatively high distance from the surface. This lack of information pertaining to the onset of erosion during spacecraft landings motivates the primary objective of this paper, which is to document the altitude at which surface erosion was first observed for both the MSL and Mars 2020 missions (Table 1). These values are calculated based on observed surface erosion in images acquired by the Mars Descent Imager (MARDI) [25] during the MSL descent, and by the rover descent camera (RDC) [26] during the Mars 2020 descent. This Technical Note is organized as follows: a summary of the MSL and Mars 2020 terminal descent propulsion system and reconstructed vehicle state is provided in Sec. II, an overview of the descent imaging systems is provided in Sec. III, and a description of the image processing techniques to determine the onset of surface erosion is provided in Sec. IV, along with images highlighting the observed surface erosion. Videos highlighting this surface modification during the MSL and M2020 descents are available as supplementary material.

II. MSL and Mars 2020 Terminal Descent Propulsion System and Vehicle State

The Mars 2020 mission was a build-to-print version of the MSL mission (Mars 2020 even flew the MSL flight-spare Descent Stage primary structure). Therefore, the Entry, Descent, & Landing (EDL) systems and architecture were nominally the same between the two missions. However, one primary difference between MSL and Mars 2020 was the addition of Terrain Relative Navigation (TRN) for Mars

Received 31 March 2023; revision received 11 August 2023; accepted for publication 5 September 2023; published online 28 September 2023.

*Assistant Professor, Department of Mechanical Engineering, Edwin A. Stevens Hall, Room E209, 1 Castle Point Terrace; jrabinov@stevens.edu. Senior Member AIAA.
†Undergraduate Student, Department of Mechanical Engineering, Carnegie Laboratory, Room 213, 1 Castle Point Terrace.
‡Supervising Engineer, 21 Enterprise Parkway, Suite 300. Associate Fellow AIAA.
§Propulsion Engineer, JPL Propulsion and Fluid Flight Systems, 4800 Oak Grove Drive. Senior Member AIAA.
¶Research Scientist, Planetary Geosciences Group, 4800 Oak Grove Drive.
**Propulsion Engineer, JPL Propulsion and Fluid Flight Systems, 4800 Oak Grove Drive.
††Physicist, Natural Environments Branch, Martin Rd SW.
‡‡Subject Matter Expert, Aerothermodynamics, Aerosciences Branch, Martin Rd SW. Senior Member AIAA.
§§Aerospace Engineer, Atmospheric Flight and Entry Systems Branch, M/S 489, 1 NASA Drive. Senior Member AIAA.

Table 1 Observed altitude for onset of surface modification for both the MSL and Mars 2020 missions

Mission	Altitude of first observed erosion (above ground level)	Descent imaging system	Image no.	Spacecraft clock time (nominal), s
MSL	70 ± 5 m	Mars descent imager (MARDI) [25]	525	397,502,121.00
Mars 2020	$64 + 6/-5$ m	Rover descent camera (RDC) [26]	4849	666,952,915.5038

Table 2 Best estimate of Mars atmospheric properties during onset of erosion

Mission	Spacecraft clock time, s	Pressure, Pa	Density, kg/m^3	Temperature, K
MSL [31]	397,502,121.00	680 ± 30	$0.0149 \pm .0006$	240 ± 20
Mars 2020 [32]	666,952,915.5038	725 ± 3	$0.01611 \pm .00007$	235 ± 1

Table 3 Best estimate of propulsion performance (individual MLE thrust values) during onset of erosion

		Reconstructed thrust estimate, N							
Mission	Spacecraft clock time, s	MLE1	MLE2	MLE3	MLE4	MLE5	MLE6	MLE7	MLE8
MSL [10]	397,502,121.00	1710 ± 50	1830 ± 50	1750 ± 50	1620 ± 50	1720 ± 50	1860 ± 50	1860 ± 50	1700 ± 50
Mars 2020 [30]	666,952,915.50	2090 ± 70	2240 ± 60	2190 ± 60	1990 ± 70	2110 ± 70	2230 ± 60	2190 ± 60	2020 ± 70

MLEs 2, 3, 6, and 7 are at a 5° cant angle, and MLEs 1, 4, 5, and 8 are at a 22.5° cant angle.

Table 4 Summary of MARDI and RDC camera performance taken from [25,26]

Camera	Location on rover	Frame rate, fps	Horizontal field of view	Vertical field of view	Image size (pixels)
MARDI [25]	Bottom-left front side of the rover	4	~70°	~52°	1600×1200
RDC [26]	Bottom-right front side of the rover	30	~35°	~30°	1280×1024

2020 [17,20]. After each mission jettisoned its parachute, powered descent was required to further slow the vehicles down so that an acceptable touchdown velocity could be realized. A detailed description of the MSL propulsion system along with a performance reconstruction is found in [10,27,28]. Each spacecraft had eight MLEs (the thrusters used for powered descent) in total mounted to the Descent Stage: four MLEs were canted with a 5° outboard angle, and the remaining four MLEs were canted with a 22.5° outboard angle [10]. A summary of the MLE performance parameters at 100% throttle can be found in Table 1 in [29]. Table 2 summarizes atmospheric parameters and Table 3 summarizes MSL and Mars 2020 thrust levels [10,27,28,30] during the altitude associated with the first observation of surface erosion; the reconstructed MLE thrust values show that the MLEs were not commanded to 100% thrust at this point. For both MSL and Mars 2020, the magnitude of spacecraft vertical velocities was <25 m/s, horizontal velocities were <0.2 m/s, horizontal and vertical accelerations were <6 m/s^2, and the planet relative angles of attack (the angle between the unit vector oriented toward the front of the rover and the planet-relative velocity unit vector) were <0.5° [31,32]. These parameters are useful for future missions interested in determining when future spacecraft designs may expect to observe surface modification during powered descent, and these parameters are also needed by the modeling community if there is interest to simulate these flow conditions.

III. MSL and Mars 2020 Descent Imaging Systems

The MARDI imager on MSL and the RDC on Mars 2020 were both capturing images during the descent of the spacecraft. Both were mounted on the rover oriented downward (toward the surface), and detailed information about the instrument capabilities and performance can be found in [25,26]. As MARDI was a science instrument, all data are archived in the Planetary Data System (PDS), and descent-specific MARDI images are publicly available.[¶] The RDC on Mars 2020 was a technology demonstration; as such, its data are not archived in PDS, but all images are also publicly available.[***] Relevant camera properties are summarized in Table 4.

IV. Image Processing

To estimate the altitude when the first erosion of the Martian surface was observed during the descent phase of the MSL and Mars 2020 missions, an image subtraction approach is used to highlight surface erosion (this technique is similar to those used in other investigations interested in visualizing Martian dust [33]). The geometrically linearized (rectified) MARDI images and the raw RDC images were used to analyze the terminal descent of the MSL and Mars 2020 missions. Figure 1 shows a visualization of the image processing steps described by Algorithm 1, with two sample RDC image frames. All image processing is performed in Python using the OpenCV library [34], and a plain word explanation of the image processing algorithm is provided below.

Image registration based on feature recognition was applied to align the Mars 2020 RDC images to the same coordinate system in order to account for the motion of the spacecraft relative to the surface during descent. The registration algorithm can account for translation, rotation, and warp between frames. It was adapted to iteratively register the images, and a total of 56 frames surrounding the onset of erosion were registered to a common reference frame. Registration was not applied to the MSL MARDI images due to the lower frame rate of this dataset and the limited amount of spacecraft/ground relative motion at times close to the first observed erosion.

The RDC images were acquired at ~30 fps (an average of 0.0335 s between each frame was calculated postflight), and the MARDI images were taken at 4 fps. To ensure that sufficient surface modification occurred between image subtraction pairs, RDC images that are eight frames apart in time are subtracted from each other

[¶]Data available online at https://pds-imaging.jpl.nasa.gov/data/msl/MSLMRD_0001/DATA/RDR/SURFACE/.

[***]Data available online at https://mars.nasa.gov/mars2020/multimedia/raw-images/.

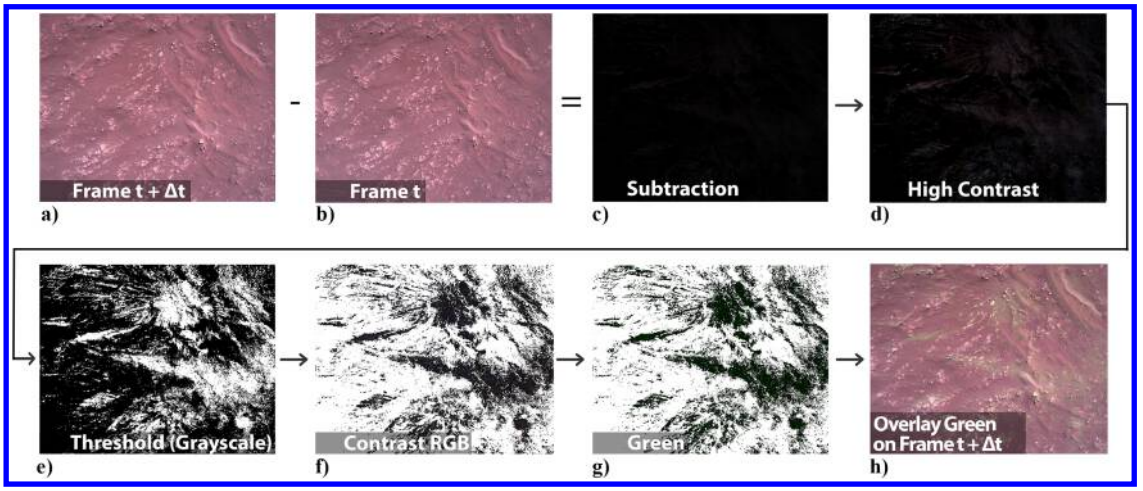

Fig. 1 Step-by-step visualization of the image processing algorithm used to highlight surface modification. Sample RDC images shown correspond to $|\mathrm{RDC}_{4865} - \mathrm{RDC}_{4857}|$.

Algorithm 1 Image subtraction algorithm for RDC images

Input: registered_RDC_Images
Output: overlayed_image
function VISUALIZE_SURFACE_EROSION(registered_RDC_Images)
for n in range(registered_RDC_Images) **do**
sub ← *subtrack*(registered_RDC_Images($n + 8$), registered_RDC_Images(n))
contrast ← *convertScaleAbs*(sub, increase contrast, no brightness change)
threshold ← *threshold*(BGRtoGrayscale(contrast), intensity range)
b,g,r ← *split*(contrast)
colored_Img ← *merge*([r, g, b, threshold])
colored_Img[:,:, redChannel] ← 0
colored_Img[:,:, blueChannel] ← 0
new_Image_Overlay ← *addWeighted*(colored_Img, registered_RDC_Images(n+8))
end for
return new_Image_Overlay
end function

The same algorithm is used for the MARDI images, though the subtraction is performed between images $n + 1$ and n, and no image registration is required.

(0.27 s between frames), which is close to matching the time difference between MARDI images (0.25 s). Once an image subtraction is performed ($|\mathrm{MARDI}_{n+1} - \mathrm{MARDI}_n|$ or $|\mathrm{RDC}_{n+8} - \mathrm{RDC}_n|$, where the subscript refers to the integer image number where sequential images are separated by a time 1/fps), the contrast value of each subtracted image was maximized within the limit of OpenCV's convertScalesAbs function, and a threshold was applied to create a green channel overlay for pixels that fell within a specified intensity range. This overlay was visualized over the MARDI_{n+1} image or the RDC_{n+8} image for the MSL and Mars 2020 datasets.

V. First Observations of Surface Erosion

After the image processing algorithm described in the previous section was applied to the MARDI and RDC datasets, it was determined that the first observable surface modification can be seen in MARDI frame 525, and in RDC frame 4849 (associated Spacecraft Clock Times are shown in Table 1). Confirmation that these frames contained evidence of surface erosion and not numerical artifacts was performed through visual inspection. A conservative altitude error estimate is included in Table 1, which corresponds to the reconstructed altitude of the spacecraft at the time associated with $\mathrm{MARDI}_{525\pm1}$ images for MSL, and $\mathrm{RDC}_{4849\pm8}$ images for Mars 2020. Figure 2 highlights the erosion that can be observed at the times presented in Table 1. Figure 3 shows more significant erosion during the MSL and Mars 2020 descents at 0.25 and 0.53 s, respectively, after the first observed erosion. While it is possible to observe the initial formation of two distinct areas of erosion in the MARDI images (Fig. 3, left), no distinct areas of erosion is observed during the Mars 2020 descent (Fig. 3, right). However, it should be noted that the image field of view differs greatly between the two cameras, and the area of erosion observed during MSL descent is larger than the entire field of view of the RDC. Analysis of surface erosion postlanding for MSL can be found in [35,36]. In Figs. 2 and 3, the markings (x) indicate the approximate location where the MLE nozzle centerlines would intersect the image plane, with the numbers corresponding to each specific MLE. The orientation of the image with respect to the rover is also noted in Figs. 2 and 3.

For MSL, from Fig. 3 (left), we can estimate a total affected area (green area) for sediment mobilization of ∼1650 m^2 (∼170 m^2 for the smaller area near the centerline impingement of MLEs 5 and 8 and ∼1500 m^2 for the area near the centerline impingement of MLEs 1, 2, 3, 4, 6, and 7). Summing the thrust values listed in Table 3 (neglecting uncertainties) gives us a total MLE thrust of 14,050 N at this point in the descent. Dividing total thrust by affected surface provides an estimate of an idealized imposed ground pressure, which gives a value of ∼9 Pa in this case. In [37], the "Blast Zone" (PSI-affected area around a spacecraft landing site) was determined for several missions, and a correlation between Blast Zone area and spacecraft thrust was presented. Using this proposed correlation from [37] of affected area = $0.02 * \mathrm{Thrust}^{1.5}$ (SI units), we get a predicted affected area for MSL Fig. 3 (left) of $(0.02\ \mathrm{m}^2/\mathrm{N}^{1.5}) \times (14,050\ \mathrm{N})^{1.5} = 33,307\ \mathrm{m}^2$. This value is roughly a factor of 2 higher than the MSL-affected area reported in [36,37], which was determined based on MSL postlanding imagery. This discrepancy is expected and is likely because the spacecraft is still at a relatively high altitude in Fig. 3, and due to viscous and turbulent dissipation along with complex jet–jet interactions, the strength of the MLE plumes has decayed significantly by the time they interact with the surface. The Blast Zone area correlation [37] was originally determined based on the total affected area throughout the entire landing phase for different missions, while Fig. 3 highlights a single snapshot in time, at a single point in the descent trajectory when surface modification has just started to occur. Furthermore, the spacecraft has a nonzero deceleration for the altitude associated with Fig. 3, so the thrust-to-weight ratio is greater than 1 (a thrust-to-weight ratio of 1 is assumed in the correlation derived in [37]). All of these reasons contribute to why the ∼1650 m^2 of affected area determined from Fig. 3 is significantly less than what was predicted by the correlation in [37].

VI. Conclusions

In this work we document for the first time the altitude of the onset of surface erosion during the descent phase of the MSL and Mars

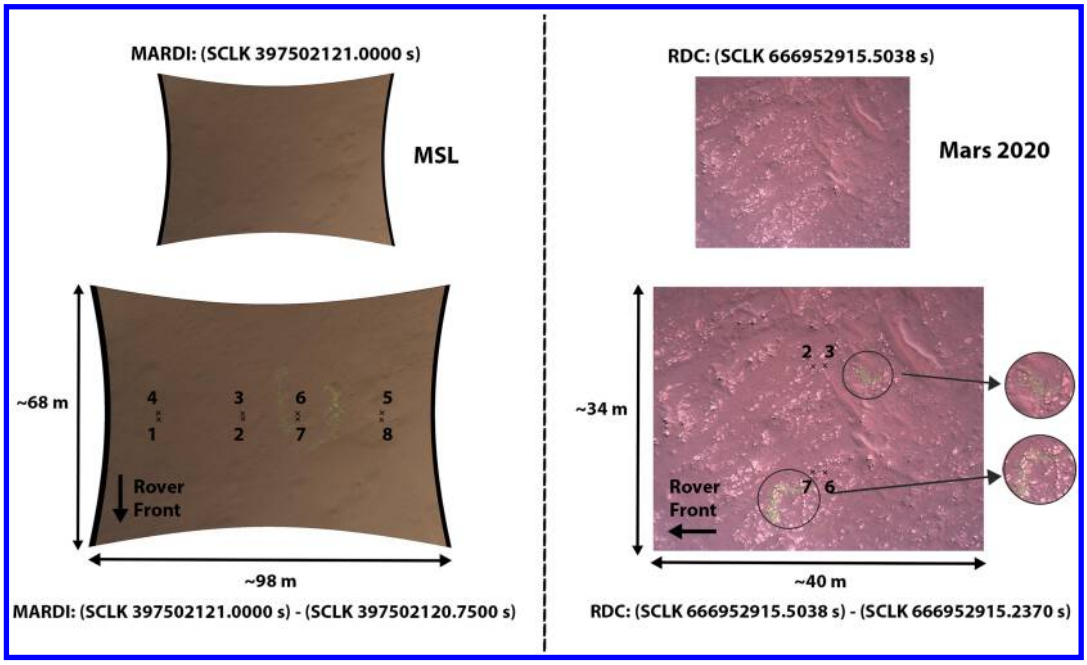

Fig. 2 Images corresponding to the first observed surface modification for both MSL and Mars 2020. The green overlay highlights the areas where surface erosion is observed using Algorithm 1. Markings (x) indicate the approximate location where the MLE nozzle centerlines would intersect the image plane, with the numbers corresponding to each specific MLE.

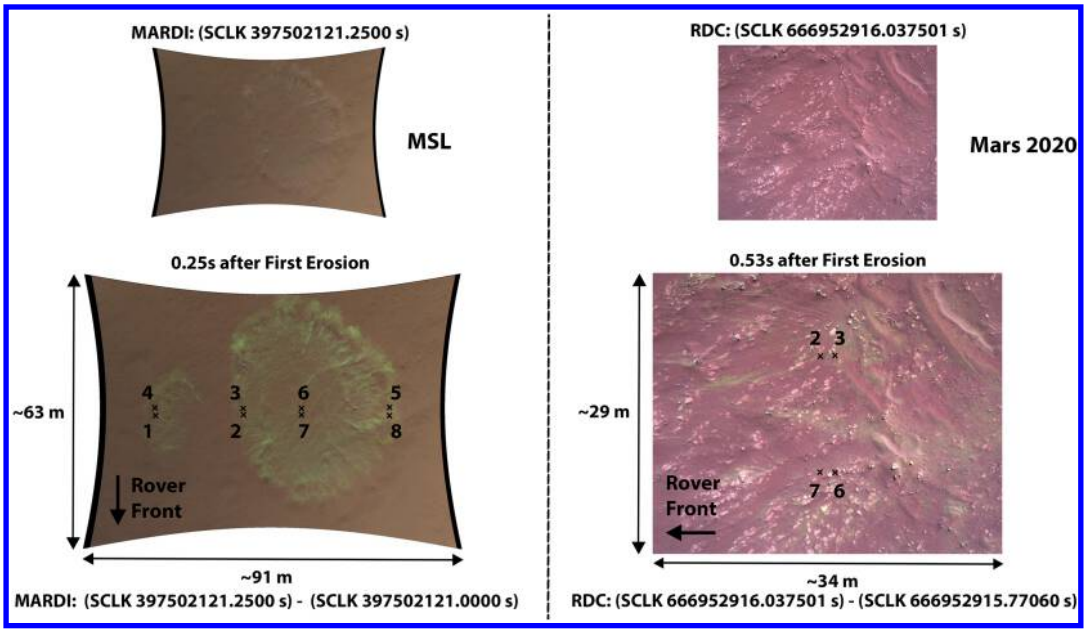

Fig. 3 Images corresponding to more significant erosion as the spacecraft descends. The green overlay highlights the areas where surface erosion is observed using Algorithm 1. Markings (x) indicate the approximate location where the MLE nozzle centerlines would intersect the image plane, with the numbers corresponding to each specific MLE.

2020 missions. Surface modification is observed at 70 ± 5 m during the MSL descent, and at $64 + 6/-5$ m during the Mars 2020 descent. A similar altitude is observed between the two missions, even though each mission targeted different landing sites with different geological properties. In the Apollo 11, 12, 16, and 17 mission reports, surface obscuration and/or dust mobilization was first reported at heights above the lunar surface of approximately 100 ft (30 m), 175 ft (53 m), 80 ft (24 m), and 60–70 ft (18–21 m), respectively [12–15].

This altitude has important engineering implications, as it determines when surface movement may start to be an error source for radar-based altitude measurements, or for image-based control algorithms such as Terrain Relative Navigation. Furthermore, this altitude and the observed erosion patterns can be used as a QOI when to comparing high-fidelity simulations to flight-data for predicting plume-induced environments during descent.

Acknowledgments

Authors Jason Rabinovitch and Soleil A. Santana acknowledge funding support through NASA Shared Services Center (NSSC) Grant Number 80NSSC21 K0899. Soleil A. Santana acknowledges funding support from the New Jersey Opportunity Meets Innovation Challenge Grant at Stevens Institute of Technology. Parts of this work were performed at the Jet Propulsion Laboratory, California Institute of Technology, under a contract with NASA. Government sponsorship acknowledged. The authors would like to thank Eric Slimko and

Andres Huertas (Jet Propulsion Laboratory, California Institute of Technology) for many enriching conversations about plume–surface interactions, and for original image-processing ideas. The authors would also like to thank two anonymous peer reviewers for taking the time to review this paper and to provide their feedback.

References

[1] Golombek, M., Grant, J., Kipp, D., Vasavada, A., Kirk, R., Fergason, R., Bellutta, P., Calef, F., Larsen, K., Katayama, Y., et al., "Selection of the Mars Science Laboratory Landing Site," *Space Science Reviews*, Vol. 170, Sept. 2012, pp. 641–737. https://doi.org/10.1007/s11214-012-9916-y

[2] Grant, J. A., Golombek, M. P., Wilson, S. A., Farley, K. A., Williford, K. H., and Chen, A., "The Science Process for Selecting the Landing Site for the 2020 Mars Rover," *Planetary and Space Science*, Vol. 164, Dec. 2018, pp. 106–126. https://doi.org/10.1016/j.pss.2018.07.001

[3] Farley, K. A., Stack, K. M., Shuster, D. L., Horgan, B. H. N., Hurowitz, J. A., Tarnas, J. D., Simon, J. I., Sun, V. Z., Scheller, E. L., Moore, K. R., et al., "Aqueously Altered Igneous Rocks Sampled on the Floor of Jezero Crater, Mars," *Science*, Vol. 377, No. 6614, 2022, Paper eabo2196. https://doi.org/10.1126/science.abo2196

[4] Martínez, G. M., Sebastián, E., Vicente-Retortillo, A., Smith, M. D., Johnson, J. R., Fischer, E., Savijärvi, H., Toledo, D., Hueso, R., Mora-Sotomayor, L., et al., "Surface Energy Budget, Albedo, and Thermal Inertia at Jezero Crater, Mars, as Observed from the Mars 2020 MEDA Instrument," *Journal of Geophysical Research: Planets*, Vol. 128, No. 2, 2023, Paper e2022 JE007537. https://doi.org/10.1029/2022 JE007537

[5] Minitti, M. E., Kah, L. C., Yingst, R. A., Edgett, K. S., Anderson, R. C., Beegle, L. W., Carsten, J. L., Deen, R. G., Goetz, W., Hardgrove, C., et al., "MAHLI at the Rocknest Sand Shadow: Science and Science-Enabling Activities," *Journal of Geophysical Research: Planets*, Vol. 118, No. 11, 2013, pp. 2338–2360. https://doi.org/10.1002/2013 JE004426

[6] Vaughan, A., Minitti, M. E., Cardarelli, E. L., Johnson, J. R., Kah, L. C., Pilleri, P., Rice, M. S., Sephton, M., Horgan, B. H. N., Wiens, R. C., et al., "Regolith of the Crater Floor Units, Jezero Crater, Mars: Textures, Composition, and Implications for Provenance," *Journal of Geophysical Research: Planets*, Vol. 128, No. 3, 2023, Paper e2022 JE007437. https://doi.org/10.1029/2022 JE007437

[7] Vasavada, A. R., Piqueux, S., Lewis, K. W., Lemmon, M. T., and Smith, M. D., "Thermophysical Properties Along Curiosity's Traverse in Gale Crater, Mars, Derived from the REMS Ground Temperature Sensor," *Icarus*, Vol. 284, March 2017, pp. 372–386. https://doi.org/10.1016/j.icarus.2016.11.035

[8] Williams, R. M. E., Grotzinger, J. P., Dietrich, W. E., Gupta, S., Sumner, D. Y., Wiens, R. C., Mangold, N., Malin, M. C., Edgett, K. S., Maurice, S., et al., "Martian Fluvial Conglomerates at Gale Crater," *Science*, Vol. 340, No. 6136, 2013, pp. 1068–1072. https://doi.org/10.1126/science.1237317

[9] Yingst, R. A., Kah, L. C., Palucis, M., Williams, R. M. E., Garvin, J., Bridges, J. C., Bridges, N., Deen, R. G., Farmer, J., Gasnault, O., et al., "Characteristics of Pebble- and Cobble-Sized Clasts Along the Curiosity Rover Traverse from Bradbury Landing to Rocknest," *Journal of Geophysical Research: Planets*, Vol. 118, No. 11, 2013, pp. 2361–2380. https://doi.org/10.1002/2013 JE004435

[10] Baker, R. S., Casillas, A. R., Guernsey, C. S., and Weiss, J. M., "Mars Science Laboratory Descent-Stage Integrated Propulsion Subsystem: Development and Flight Performance," *Journal of Spacecraft and Rockets*, Vol. 51, No. 4, 2014, pp. 1217–1226. https://doi.org/10.2514/1.A32788

[11] Roberts, L., "The Interface of a Rocket Exhaust with the Lunar Surface," *Fluid Dynamic Aspects of Space Flight*, Vol. 2, New York Gordon and Breach Science Publishers, 1966, pp. 269–290.

[12] NASA Mission Evaluation Team, "Apollo 11 Mission Report: Preflight, Flight, and Postflight of Apollo 11," NASA TM MSC-00171, Nov. 1969, https://ntrs.nasa.gov/archive/nasa/casi.ntrs.nasa.gov/19700008096.pdf.

[13] NASA Mission Evaluation Team, "Apollo 12 Mission Report," NASA TM MSC-01855, March 1970, https://ntrs.nasa.gov/archive/nasa/casi.ntrs.nasa.gov/19760072997.pdf.

[14] NASA Mission Evaluation Team, "Apollo 16 Mission Report," NASA TM MSC-07230, Aug. 1972, https://ntrs.nasa.gov/archive/nasa/casi.ntrs.nasa.gov/19720026127.pdf.

[15] NASA Mission Evaluation Team, "Apollo 17 Mission Report," NASA TM JSC-07904, March 1973, https://ntrs.nasa.gov/archive/nasa/casi.ntrs.nasa.gov/19730015117.pdf.

[16] Soffen, G. A., "The Viking Project," *Journal of Geophysical Research (1896–1977)*, Vol. 82, No. 28, 1977, pp. 3959–3970. https://doi.org/0.1029/JS082i028p03959

[17] Prakash, R., Burkhart, P. D., Chen, A., Comeaux, K. A., Guernsey, C. S., Kipp, D. M., Lorenzoni, L. V., Mendeck, G. F., Powell, R. W., Rivellini, T. P., et al., "Mars Science Laboratory Entry, Descent, and Landing System Overview," *IEEE Aerospace Conference*, IEEE, New York, 2008, pp. 1–18.

[18] Sengupta, A., Kulleck, J., Van Norman, J., and Mehta, M., "Thermal Coating Erosion in a Simulated Martian Landing Environment," *Wear*, Vol. 270, No. 5, 2011, pp. 335–343. https://doi.org/10.1016/j.wear.2010.09.013

[19] Bradford, E., Rabinovitch, J., and Abid, M., "Regolith Particle Erosion of Material in Aerospace Environments," *IEEE Aerospace Conference*, IEEE, New York, 2019, pp. 1–15.

[20] Nelessen, A., Sackier, C., Clark, I., Brugarolas, P., Villar, G., Chen, A., Stehura, A., Otero, R., Stilley, E., Way, D., et al., "Mars 2020 Entry, Descent, and Landing System Overview," *IEEE Aerospace Conference*, IEEE, New York, 2019, pp. 1–20.

[21] Chen, C. W., and Pollard, B. D., "Radar Terminal Descent Sensor Performance During Mars Science Laboratory Landing," *Journal of Spacecraft and Rockets*, Vol. 51, No. 4, 2014, pp. 1208–1216. https://doi.org/10.2514/1.A32641

[22] Johnson, A. E., Aaron, S. B., Ansari, H., Bergh, C., Bourdu, H., Butler, J., Chang, J., Cheng, R., Cheng, Y., Clark, K., et al., "Mars 2020 Lander Vision System Flight Performance," *AIAA SCITECH Forum*, AIAA Paper 2022-1214, Jan. 2022.

[23] Capecelatro, J., "Modeling High-Speed Gas-Particle Flows Relevant to Spacecraft Landings," *International Journal of Multiphase Flow*, Vol. 150, May 2022, Paper 104008. https://doi.org/10.1016/j.ijmultiphaseflow.2022.104008

[24] Balakrishnan, K., and Bellan, J., "High-Fidelity Modeling and Numerical Simulation of Cratering Induced by the Interaction of a Supersonic Jet with a Granular Bed of Solid Particles," *International Journal of Multiphase Flow*, Vol. 99, Feb. 2018, pp. 1–29. https://doi.org/10.1016/j.ijmultiphaseflow.2017.08.008

[25] Malin, M. C., Ravine, M. A., Caplinger, M. A., Tony Ghaemi, F., Schaffner, J. A., Maki, J. N., Bell, J. F., III, Cameron, J. F., Dietrich, W. E., Edgett, K. S., et al., "The Mars Science Laboratory (MSL) Mast Cameras and Descent Imager: Investigation and Instrument Descriptions," *Earth and Space Science*, Vol. 4, No. 8, 2017, pp. 506–539. https://doi.org/10.1002/2016EA000252

[26] Maki, J. N., Gruel, D., McKinney, C., Ravine, M. A., Morales, M., Lee, D., Willson, R., Copley-Woods, D., Valvo, M., Goodsall, T., et al., "The Mars 2020 Engineering Cameras and Microphone on the Perseverance Rover: A Next-Generation Imaging System for Mars Exploration," *Space Science Reviews*, Vol. 216, No. 137, 2020, pp. 1–48. https://doi.org/10.1007/s11214-020-00765-9

[27] Guernsey, C. S., and Weiss, J. M., "Lessons Learned from the Development of the MSL Descent Stage Propulsion System," *AAS/AIAA Spaceflight Mechanics Meeting*, American Astronautical Soc. Paper 2013-457, 2013.

[28] Jeffrey, W., and Guernsey, C., "Design and Development of the MSL Descent Stage Propulsion System," *Space Flight Mechanics Meeting*, American Astronautical Soc. Paper 2013-458, 2013.

[29] Mehta, M., Sengupta, A., Renno, N. O., Norman, J. W. V., Huseman, P. G., Gulick, D. S., and Pokora, M., "Thruster Plume Surface Interactions: Applications for Spacecraft Landings on Planetary Bodies," *AIAA Journal*, Vol. 51, No. 12, 2013, pp. 2800–2818. https://doi.org/10.2514/1.J052408

[30] Turner, D., Jens, E., and Casillas, A., "Mars 2020 Descent Stage Integrated Propulsion Subsystem: Changes from MSL and Flight Performance" (Under Review).

[31] Karlgaard, C. D., Kutty, P., Schoenenberger, M., Munk, M. M., Little, A., Kuhl, C. A., and Shidner, J., "Mars Science Laboratory Entry Atmospheric Data System Trajectory and Atmosphere Reconstruction," *Journal of Spacecraft and Rockets*, Vol. 51, No. 4, 2014, pp. 1029–1047. https://doi.org/10.2514/1.A32770

[32] Karlgaard, C. D., Schoenenberger, M., Dutta, S., and Way, D. W., "Mars Entry, Descent, and Landing Instrumentation 2 Trajectory, Aerodynamics, and Atmosphere Reconstruction," *Journal of Spacecraft and Rockets*, Vol. 60, No. 1, 2023, pp. 199–214. https://doi.org/10.2514/1.A35440

[33] Lemmon, M. T., Lorenz, R. D., Rabinovitch, J., Newman, C. E., Williams, N. R., Sullivan, R., Golombek, M. P., Bell, J. F., III, Maki, J. N., and Vicente-Retortillo, A., "Lifting and Transport of Martian

Dust by the Ingenuity Helicopter Rotor Downwash as Observed by High-Speed Imaging From the Perseverance Rover," *Journal of Geophysical Research: Planets*, Vol. 127, No. 12, 2022, Paper e2022 JE007605.
https://doi.org/10.1029/2022 JE007605

[34] Bradski, G., "The OpenCV Library," *Dr. Dobb's Journal of Software Tools*, 2000, https://github.com/opencv/opencv/wiki/CiteOpenCV.

[35] Vizcaino, J., and Mehta, M., "Quantification of Plume-Soil Interaction and Excavation due to the Mars Science Laboratory Sky Crane Descent Phase," *8th Symposium on Space Resource Utilization*, AIAA Paper 2015-1649, 2015.

[36] Arvidson, R. E., Bellutta, P., Calef, F., Fraeman, A. A., Garvin, J. B., Gasnault, O., Grant, J. A., Grotzinger, J. P., Hamilton, V. E., Heverly, M., et al., "Terrain Physical Properties Derived from Orbital Data and the First 360 Sols of Mars Science Laboratory Curiosity Rover Observations in Gale Crater," *Journal of Geophysical Research: Planets*, Vol. 119, No. 6, 2014, pp. 1322–1344.
https://doi.org/10.1002/2013 JE004605

[37] Lorenz, R. D., "Lander Rocket Exhaust Effects on Europa Regolith Nitrogen Assays," *Planetary and Space Science*, Vol. 127, Aug. 2016, pp. 91–94.
https://doi.org/10.1016/j.pss.2016.04.008

K. T. Edquist
Associate Editor